MATERIALS CHEMISTRY FRONTIERS

RESEARCH ARTICLE

View Article Online
View Journal

Cite this: DOI: 10.1039/d6qm00041j

Double decker NHC-cyclometallated Pt complexes for highly-efficient vacuum-deposited green OLEDs and NIR emission

Irene Melendo, [a] Lucy A. Weatherill, [b] Antonio Martín, [a] Piotr Pander, [cd] Fernando B. Dias, *[b] Sara Fuertes *[a] and Violeta Sicilia *[e]

The dinuclear compound [{Pt^{II}(C^C*)(μ-N^N)}$_2$] (HN^N: diphenylformamidine; HC^C* = 3-methyl-1-(naphthalen-2-yl)-1*H*-imidazol-2-ylidene, **3**) was obtained as a pure single *anti*-isomer, with a Pt–Pt distance of 2.8645 Å. Under UV light, **3** reacted with haloforms to obtain the corresponding oxidized species [{Pt^{III}(C^C*)(μ-N^N)X}$_2$] (**4-X**). X-ray analysis of **4-Cl** confirmed the retention of the *anti*-conformation and revealed a shortened Pt–Pt distance (2.6070 Å) consistent with metal–metal bonding in the Pt$_2$(III,III) system. In addition, methylation of the electron-rich complex **3** with [Me$_3$O]BF$_4$ provided the mixed-valence dinuclear species [(C^C*)Pt^{II}(μ-N^N)$_2$Pt^{IV}(C^C*)(CH$_3$)]BF$_4$ (**5**), which exhibits two distinct ^{195}Pt NMR resonances (δ: −2373 and −3264 ppm) and a large Pt–Pt coupling constant (2155 Hz). Compound **3** shows a structureless emission band at 520 nm in 2 wt% PMMA (poly(methyl methacrylate)) film, with a photoluminescence decay of 1.80 μs and quantum yield of 0.90, typical of triplet metal–metal–to-ligand charge transfer (^{3}MMLCT) [dσ*(Pt–Pt) → π*(C^C*)] excited states. The oxidized counterparts, **4-X**, display phosphorescent emissions with maxima at 960, 970 and 1055 nm in solid state at 77 K. These are tentatively assigned to triplet axial ligand-to-metal–metal charge transfer (^{3}XMMCT) [σ(X) → dσ*(Pt–Pt)]. Whilst complex **5** shows no emission in either the visible or near-infrared regions at 298 or 77 K. Organic light-emitting diodes (OLEDs) incorporating **3** as a green emitter demonstrate excellent device performance, achieving a turn-on voltage of 3 V, an external quantum efficiency (EQE) reaching 22% and a maximum luminance exceeding 22 000 cd m^{-2}.

Received 19th January 2026,
Accepted 15th March 2026

DOI: 10.1039/d6qm00041j

rsc.li/frontiers-materials

Introduction

Beyond their widespread use in conventional solid-state lighting, OLEDs have become instrumental to a new generation of advanced technologies.[1–3] In particular, their exceptional image quality, ultrathin design and mechanical flexibility have enabled their integration into portable flat-panel displays,[4,5] ultralight wearable systems embedded in textiles[6,7] and, lately, implantable biomedical electronics.[8,9]

Nevertheless, the development of key OLED components like the emissive materials remains crucial for enhancing device stability and electroluminescent efficiency.[10,11] In this sense, there has been recently a growing interest in designing bimetallic complexes for optoelectronic applications.[12–14] Incorporating a second metal atom in the structure is expected to enhance the spin–orbit coupling (SOC) and increase the radiative decay rate constant. Thereby this should lead to shorter emission lifetimes and higher quantum yields (QY), ultimately improving their efficiency as OLED emitters.[15,16] Within this class of bimetallic emitters, Pt(II)-based systems hold a leading position due to the rich and tunable photophysical properties derived from the inherent square planar coordination geometry. A key structural feature of d^8 complexes is the presence of an open axial site, *z*-direction, which strongly predisposes them to maintain short Pt···Pt contacts, giving rise to ^{3}MMLCT states. These are often characterized by bathochromically shifted emission bands, making them especially attractive for the design of red-to-near infrared (NIR) luminophores, which generally suffer from lower photoluminescent QY. This limitation partially comes from the exponential increase in

[a] *Instituto de Síntesis Química y Catálisis Homogénea (ISQCH), CSIC - Universidad de Zaragoza, Pedro Cerbuna 12, 50009, Zaragoza, Spain. E-mail: s.fuertes@csic.es*
[b] *Department of Physics, Durham University, SouthRoad, Durham, DH1 3LE, UK. E-mail: f.m.b.dias@durham.ac.uk*
[c] *Faculty of Chemistry, Silesian University of Technology, M. Strzody 9, 44-100 Gliwice, Poland*
[d] *Centre for Organic and Nanohybrid Electronics, Silesian University of Technology, Konarskiego 22B, 44-100 Gliwice, Poland*
[e] *Departamento de Química Inorgánica, Escuela de Ingeniería y Arquitectura de Zaragoza, ISQCH, CSIC – Universidad de Zaragoza, Campus Río Ebro, Edificio Torres Quevedo, 50018, Zaragoza, Spain. E-mail: sicilia@unizar.es*

nonradiative decay rates as the T_1–S_0 energy gap decreases, due to the electron-vibrational coupling between these two manifolds.[17] Alternative approaches, such as thermally activated delayed fluorescence (TADF) emitters have also been explored to overcome the intrinsic efficiency limitations of these low energy emissions. By designing molecules with a small singlet–triplet energy gap, reverse intersystem crossing enables efficient harvesting of triplet excitons. Donor–acceptor architectures, extended π-conjugation, and rigid frameworks have successfully pushed TADF emission into the deep red and even NIR regions.[18–20] Even so, achieving simultaneously long-wavelength emission, high quantum yields, and operational stability remains challenging, especially in the solid state.

To mitigate these photophysical drawbacks, molecular architectures such as double-decker systems with cycloplatinated ligands and strongly bonded bridging groups have become a well-established strategy.[12,21,22] They offer a semirigid dinuclear scaffold with short metal–metal separations, which reduces excited-state distortions while enabling highly efficient, low-lying emissions. These can be modulated through molecular design, particularly by modifying the cyclometallated and/or auxiliary bridging ligands.

To date, only a handful of light-emitting devices based on Pt complexes doubly bridged by 4-bond units have been reported in the literature.[23–36] Most of these Pt emitters incorporate chromophoric C^N-cyclometallated ligands together with mercapto-N-heterocycles in their molecular structure and are typically formulated as $[\{Pt(C\hat{}N)(\mu\text{-}N\hat{}S)\}_2]$.[23–29] This set of devices exhibits deep red to NIR electroluminescence with relatively low EQEs, reaching only in a few of cases values of *ca.* 9%.[24,26] However, employing more structurally rigid and constrained μ_2-N^N ligands, such as α-carbolinate,[32,33] and pyridobenzoxazinide,[34] resulted in significant performance improvements, achieving EQEs of around 20% in deep red to NIR OLEDs. More recently, replacing the C^N-ligand with a cyclometallated N-heterocyclic carbene (C^C*) has afforded red and deep red emitters for vacuum-deposited OLEDs with even higher EQEs, reaching up to 21.3%[35] and 32.7%.[36]

In parallel, our previous research was focused on this type of complexes $[\{Pt(bzq)(\mu\text{-}N\hat{}S)\}_2]$ (Hbzq = benzo[*h*]-quinoline; N^SH = 2-mercaptobenzothiazole,[21] 2-mercaptobenzoxa-zolate,[37] 2-mercaptopyrimidine,[38] 4-(trifluoromethyl)-2-mercaptopyrimidine[39]), that in some cases yielded red light-emitting compounds with QY up to 0.90. Our most recent investigations have revealed further insights into these systems. We have published a series of dinuclear Pt(II) complexes with different C^N cyclometallated ligands and S^N bridging groups, $[\{Pt^{II}(C\hat{}N)(\mu\text{-}N\hat{}S^R)\}_2]$,[40,41] and their corresponding oxidized Pt(III) complexes $[\{Pt^{III}(C\hat{}N)(\mu\text{-}S\hat{}N^R)X\}_2]$ (X = Cl, Br, I). While the former, Pt_2(II,II) complexes, display the typical orangish emissions it is the oxidized Pt_2(III,III) species that are particularly remarkable, exhibiting NIR-II emissions with maxima ranging from 985 to 1215 nm.

Now, in this work, we projected the use of N-heterocyclic carbenes instead of C^N-cyclometallated ligands since they are known as photostable and very efficient Pt(II) phosphorescent emitters.[42] The fact of having two strong carbon–metal σ bonds produces a large crystal field splitting and reduces the photo- or thermal population of the non-radiative dd* excited states leading to higher emission efficiencies than the C^N counterpart.[43] With these considerations in mind, we developed a synthetic strategy to obtain the dinuclear complex $[\{Pt(C\hat{}C^*)(\mu\text{-}N\hat{}N)\}_2]$ (HC^C* = 3-methyl-1-(naphthalen-2-yl)-1*H*-imidazol-2-ylidene; HN^N: diphenylformamidine **3**) as a single *anti*-isomer. Then, the reaction of **3** with haloforms and Me_3OBF_4 afforded the two-electron-oxidized dinuclear Pt(III) complexes $[\{Pt(C\hat{}C^*)(\mu\text{-}N\hat{}N)X\}_2]$ (X = Cl (**4-Cl**), Br (**4-Br**), I (**4-I**)) and $[(C\hat{}C^*)Pt(\mu\text{-}N\hat{}N)_2Pt(C\hat{}C^*)(CH_3)]BF_4$ (**5**). X-ray diffraction, theoretical and photophysical studies were carried out on the Pt complexes. Electroluminescent devices have been fabricated using **3** as a green emitter exhibiting outstanding performance.

Results and discussion

Synthesis and characterization of platinum complexes

Inspired by our previously reported synthesis of dinuclear Pt complexes with bridging pyrazolates $[\{Pt(C\hat{}C^*)(\mu\text{-}Rpz)\}_2]$ (HC^C*: 1-(4-(ethoxycarbonyl)phenyl)-3-methyl-1*H*-imidazol-2-ylidene)[44,45] and after several attempts to prepare the targeted dinuclear Pt(II) complex $[\{Pt(C\hat{}C^*)(N\hat{}N)\}_2]$ (HC^C* = 3-methyl-1-(naphthalen-2-yl)-1*H*-imidazol-2-ylidene, HN^N = diphenylformamidine, **3**) we found out that the best starting material was complex $[Pt(C\hat{}C^*)(N\hat{}NH)_2]PF_6$ (**2**) (Scheme 1, path a). To obtain **2**, we prepared compound **1** (see experimental section in the SI and Fig. S1) Then, complex **2** was prepared by reaction of $[Pt(C\hat{}C^*)(NCMe)_2]PF_6$ (**1**) with excess (1 : 4) of *N,N′*-diphenylformamidine in methanol. After 3 h of stirring and the subsequent work-up, the cationic compound **2** was obtained as a white solid in good yield and was characterized (see Fig. S2).

The ^{1}H NMR spectrum in CD_2Cl_2 shows only one set of signals for the C^C* group and two for the non-equivalents formamidine ligands. The coordination of the formamidine ligands was manifest from the NC*H*N resonances in the ^{1}H NMR spectrum that exhibited a broad base due to ^{195}Pt

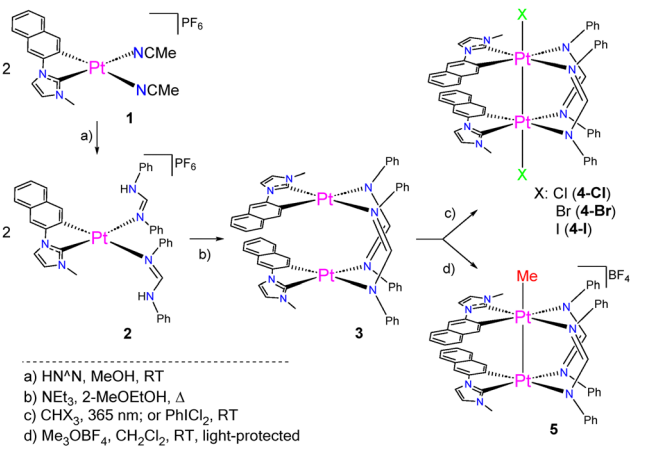

Scheme 1 Synthesis of Pt complexes.

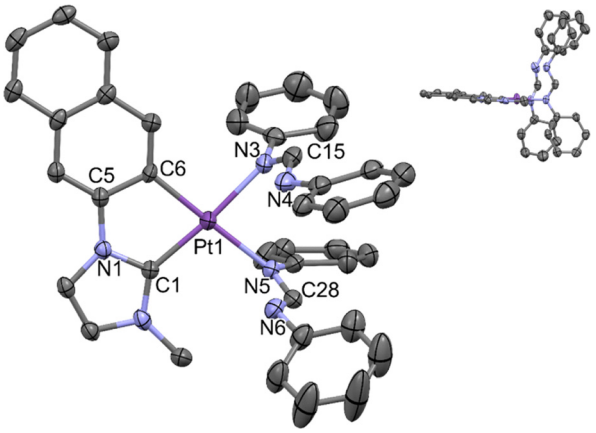

Fig. 1 X-ray molecular structure of complex **2**. Inset: Perspective view of the cationic complex. Hydrogens have been omitted for clarity. Thermal ellipsoids are drawn at their 50% probability level.

satellites. Besides that, the 2D ^{1}H-^{195}Pt NMR spectrum shows the corresponding crosspeak (see Fig. S2h) for the NC*H*N signal. X-ray diffraction analysis confirmed the proposed molecular structure of compound **2** (Fig. 1 and Table S2), revealing a Pt center in a distorted square-planar coordination environment. This distortion arises from the small bite angle (80.3(2)°) of the NHC-cyclometallated ligand. Two formamidine ligands, with the N–H oriented to the d_{z^2} orbital of the metallic center, complete its coordination sphere. The 5-membered metallocycle (Pt, C1, N1, C5, C6) is basically co-planar with the platinum coordination plane (Pt, C1, C6, N3, N5) with an interplanar angle of 2.3(2)° whereas both formamidines are located almost perpendicular to it (Pt, C1, C6, N3, N5) with dihedral angles of 82.5(6)° and 73.7(4)° for the corresponding planes defined by C16, N3, C15, N4, C22 and C29, N5, C28, N6, C35 (Inset Fig. 1). The protocol to synthesize compound **3** as a single *anti*-isomer with respect to the C^C* orientation, was successfully achieved by treatment of **2** with NEt_3 in refluxing 2-methoxyethanol (Scheme 1, path b). After processing the reaction mixture, complex **3** was obtained as a yellow solid in very good yield (77%).

While previously reported one-pot methods often involved purification by column chromatography,[31,35,46–49] our synthetic procedure offers a more straightforward work-up and delivers the dinuclear compound as a pure single isomer with consistently high yield. Complex **3** was fully characterized by multinuclear NMR spectroscopy (Fig. S3) and the molecular structure was later confirmed by X-ray diffraction (see below). Owing to their particular electronic and structural characteristics, this type of Pt(II) complexes are prone to undergo two-center two-electron oxidations in the presence of halogenated species.[38,40,50,51] In line with this behaviour, compound **3** reacts with haloforms CHX_3 (X = Cl, Br, I) upon irradiation with 365 nm light in the presence of air, affording the corresponding dihalogenated diplatinum(III) complexes $[\{Pt(C\hat{}C^*)(\mu\text{-}N\hat{}N)X\}_2]$ (X = Cl **4-Cl**, Br **4-Br**, I **4-I**) as orange, brown, and garnet solids, respectively, in moderate to good yields (42–71%). Compound **4-Cl**, could be obtained in a better yield by oxidation of **3** with $C_6H_5ICl_2$ (Scheme 1, path c). Additionally, the reaction of the electron-rich $Pt_2(II,II)$ complex **3** with trimethyloxonium tetrafluoroborate in CH_2Cl_2 at rt and protected from light resulted in an electrophilic attack by the Me group yielding the unsaturated dinuclear species $[(C\hat{}C^*)Pt(\mu\text{-}N\hat{}N)_2Pt(C\hat{}C^*)(CH_3)]BF_4$ (**5**), Scheme 1, path d. All compounds were fully characterized showing a single *anti*-conformation in all cases (Fig. S4–S7). The ^{1}H NMR spectra of symmetric complexes **3** and **4-X** show a set of signals corresponding to half of the molecule, consistent with the proposed geometry of the *anti*-isomer. In this sense, only one singlet for the methyl resonance (C^C*) is observed at *ca.* 2.30 ppm. This signal is particularly sensitive to the nature and spatial arrangement of the ligands surrounding the Pt center. In these cases, it experiences an upfield shift when compared to that of complex **2** (3.82 ppm), due to the anisotropic shielding effect of the bridging phenylformamidinates. These spectra exhibit a distinctive resonance for the proton of the bridging amidinate, NC*H*N, that seems to be chemically and magnetically equivalents in **3**, given rise to a singlet at 8.52 ppm, but magnetically inequivalent in **4-X**, regardless of the axial ligand (Fig. 2, top).

In these cases, the most intense singlet corresponds to species with both Pt centers inactive in NMR (red, ~44% of the signal). Species with only one ^{195}Pt atom (I = 1/2) cause the appearance of two sets of platinum satellites ($^{3}J_{Pt-H}$ ~76 and $^{3}J_{Pt-H}$ ~60 Hz for green and blue respectively) that correspond to 44% of the signal. Finally, approximately 11% of the signal is originated from molecules containing two ^{195}Pt centers (yellow circle) which are expected to appear as a doublet of doublets, yet the central peaks are overlapped with the main singlet. To substantiate this statement, we carried out a ^{1}H{^{195}Pt} NMR

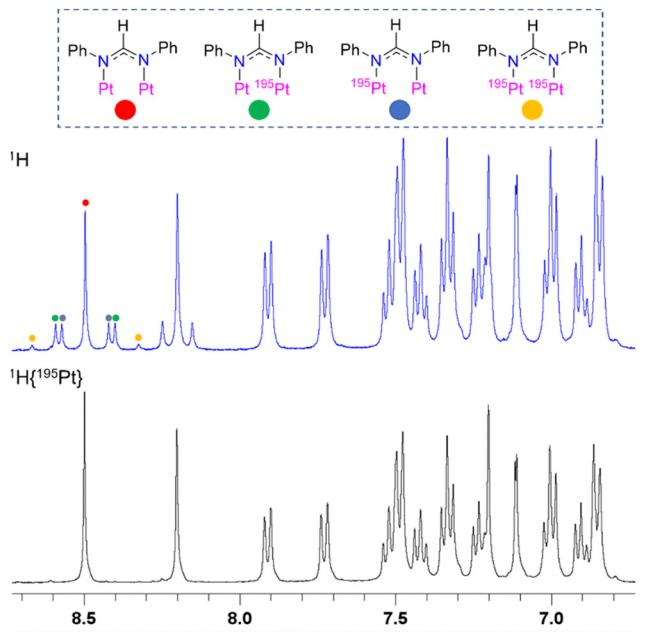

Fig. 2 Expanded view of the ^{1}H (top) and ^{1}H{^{195}Pt} (bottom) NMR spectra of **4-Cl** in CD_2Cl_2. Inset: Isotopic analysis for the NC*H*N.

experiment that exhibited the total disappearance of the platinum satellites (Fig. 2, bottom), including those for the proton of the naphthyl fragment (δ: 8.19 ppm).

The ^{195}Pt{^{1}H} NMR spectra of **3** and **4-X** show single resonances at *ca.* −3524 ppm for compound **3** (Fig. 3) and in the range −2400 to −2700 ppm for complexes **4-X**. This considerably downfield shifted ($\Delta\delta$Pt: 827–1211 ppm), is in accordance with the increased oxidation state of the metal centers, in line with previous reports.[40,41,52,53] By contrast, the ^{195}Pt{^{1}H} NMR spectrum of **5** shows two platinum resonances at δ: −2373 ppm (Pt–Me) and −3264 ppm (Pt) (Fig. 3), with a Pt–Pt coupling constant of 2155 Hz, making evident the asymmetry of this molecule along with the existence of a metal–metal bond. The δ^{195}Pt and the Pt–Pt coupling constant resemble those of complex [(C^C*)Pt^{II}(μ-pz)$_2$Pt^{IV}(C^C*)(CH$_3$)]BF$_4$ (HC^C*: 1-(4-ethoxycarbonyl)phenyl)-3-methyl-1*H*-imidazol-2-ylidene)[52] with δPt: −2589 (Pt–Me), −3064 ppm (Pt) and $^1J_{Pt-Pt}$ = 1023 Hz. Nonetheless, the Pt–Pt coupling constant of **5** appears to be much larger, 2155 Hz, indicating a stronger interaction between the Pt centers. This effect is likely due to the 4-bond bridging amidinates maintaining a more robust and rigid framework than the pyrazolate ligands.

As a final NMR remark, in complex **5**, the H of the bridging amidinate (NC*H*N) are not chemically equivalent and give rise to two different singlets at 8.69 and 8.49 ppm (see Fig. S7 and Fig. 4, bottom). The former shows two different Pt–H coupling constants of 83.9 and 40.5 Hz whereas the latter just one set of Pt satellites with a coupling constant of 59.3 Hz. In order to gain structural information, ^{1}H{^{195}Pt} NMR spectra were recorded with selective irradiation of the platinum center. As shown in Fig. 4, middle, when the experiment was conducted decoupling at δPt: −2373 ppm, the singlet at 8.69 ppm showed a single set of satellites with $^3J_{H-Pt}$ = 83.9 Hz while those associated to the 8.49 ppm resonance were attenuated in intensity but neither disappeared nor changed the coupling constant value. Alternatively, decoupling at δPt: −3264 ppm resulted in the 8.69 ppm signal displaying the other set of satellites ($^3J_{H-Pt}$ = 40.5 Hz) and those of the 8.49 ppm resonance were likewise reduced in intensity.

These observations are consistent with the splitting pattern obtained for the axial methyl group [δH = 1.64 ppm, $^2J_{Pt-H}$ = 65.7 Hz, $^3J_{Pt-H}$ = 15.6 Hz]. Accordingly, the ^{1}H NMR spectrum irradiated at −2373 ppm only exhibited the $^3J_{Pt-H}$ = 15.6 Hz coupling for the methyl resonance whereas irradiation at −3264 ppm displayed the set of Pt satellites with a larger coupling constant of $^2J_{Pt-H}$ = 65.7 Hz. Based on these NMR experiments and the great similitude to complex [(C^C*)Pt^{II}(μ-pz)$_2$Pt^{IV}(C^C*)(CH$_3$)]BF$_4$, we propose a mixed valence Pt$_2$(II,IV) formulation for complex **5** with the metals involved in a donor–acceptor Pt(II) → Pt(IV) bond.

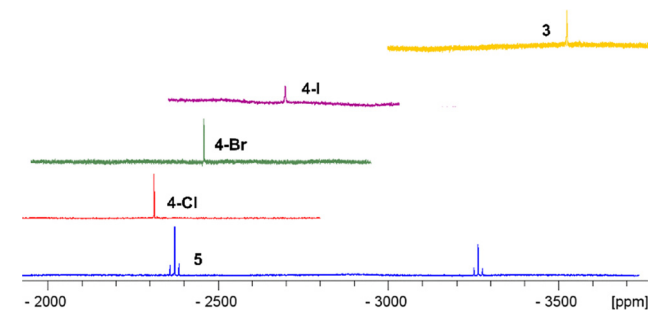

Fig. 3 ^{195}Pt{^{1}H} NMR spectra of **3**, **4-X** and **5** at 298 K.

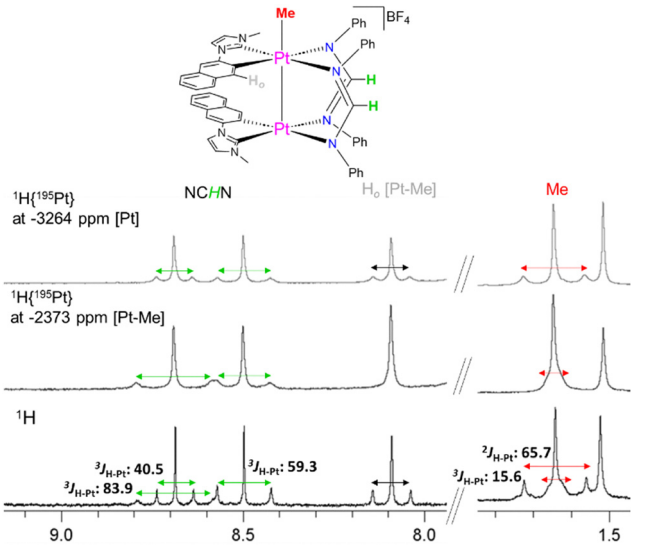

Fig. 4 Expanded view of the ^{1}H and ^{1}H{^{195}Pt} NMR spectra of **5** in CD_2Cl_2.

The X-ray molecular structures of complexes **3** and **4-Cl** have been depicted in Fig. 5. A full description along with a selection of bond distances and angles appear in the SI (Table S2 and Fig. S8). As shown in Fig. 5, complex **3** is formed by two Pt(C^C*) units doubly bridged with two fomamidinates, with the C^C* fragments displaying an *anti*-arrangement.

The metal centers are in close proximity with a Pt–Pt distance of 2.86457(17) Å, like in similar amidinate dinuclear complexes,[30,31,35,46–48,54] denoting a strong interaction of the 5d$_{z^2}$ orbitals of both platinum centers. X-ray diffraction studies on **4-Cl** and **4-I** confirmed that the oxidation of **3** proceeds with retention of the conformation, obtaining the *anti*-isomer for both complexes. The Pt(III) centers have a distorted octahedral environment with the axial positions occupied by a halogen atom and the other Pt(III) center and with the X–Pt–Pt angles being close to 177° (X: Cl). The Pt–Pt distance 2.6070(5) Å is smaller than that of complex **3**, in accordance with the presence of a metal–metal bond between both Pt(III) centers.[21,40,41,51,55,56] A deeper examination of the crystal structures revealed in **3** and **4-Cl** π–π intermolecular interactions (3.27–3.51 Å, cyan dotted lines, insets Fig. 5) between the C^C* fragments of adjacent molecules, leading to the formation of 1D-stackings. In **4-Cl**, this supramolecular array is also supported by H···Cl interactions (*d* H–Cl: 2.628 Å, *d* C–Cl: 3.464 Å) between the C^C* and the axial Cl ligands.

Photophysical, electrochemical properties and theoretical studies

Absorption properties and theoretical calculations. UV-Vis absorption spectra of complexes **2–5** were recorded in solution

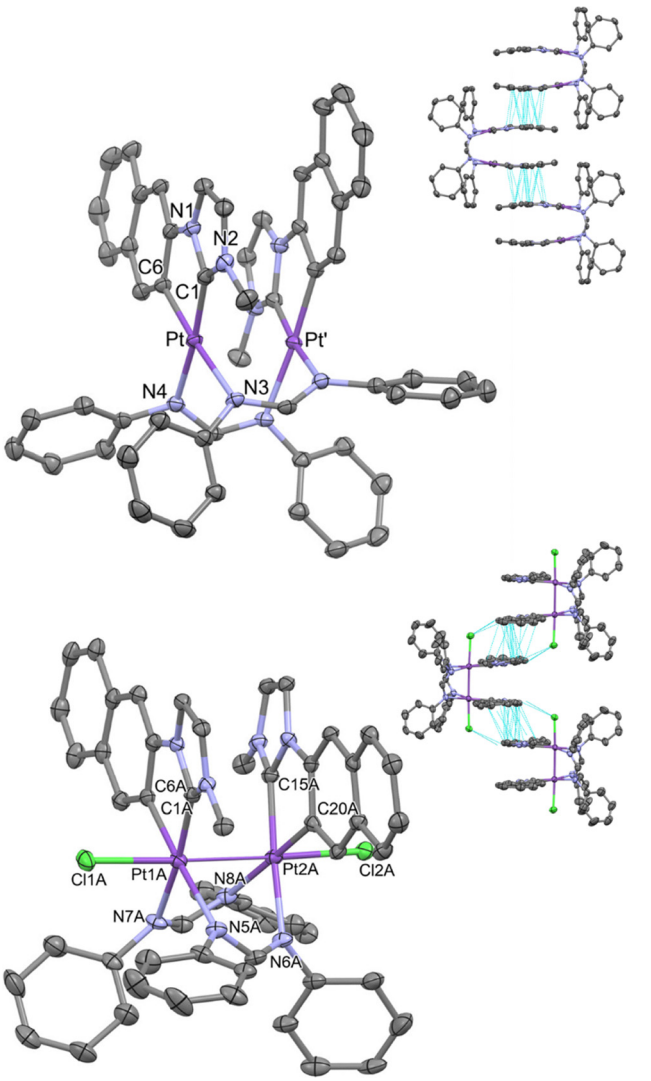

Fig. 5 X-ray molecular structures of **3** (top) and **4-Cl** (bottom). Insets: Crystal packing views. Hydrogens and solvent molecules have been omitted for clarity. Thermal ellipsoids are drawn at their 50% probability level.

at 5×10^{-5} M. The pertinent data are listed in Table S3 and represented in Fig. 6 and Fig. S9, S10. The high energy absorption bands of all complexes are typically attributed to intraligand transitions π–π*[(C^C*)]. For complex **3**, a low energy band is observed at 420 nm that follows the Beer–Lambert law within the 10^{-6} to 10^{-3} M range, indicating that no significant intermolecular ground state aggregation is observed. This band can be reasonably assigned to a ^{1}MMLCT [dσ*(Pt–Pt) → π*(C^C*)] transition. The UV-Vis spectrum of the monometallic precursor, complex **2**, shows the absence of this low energy absorption band, which strongly supports the ^{1}MMLCT assignment. The oxidized derivatives also exhibit low-energy absorptions that in the case of complex **4-I** (λ_{abs} = 468 nm) appears at much longer wavelength than in the parent complex **3**.

To provide further insights into the origin of the photophysical properties, Density Functional Theory (DFT) and

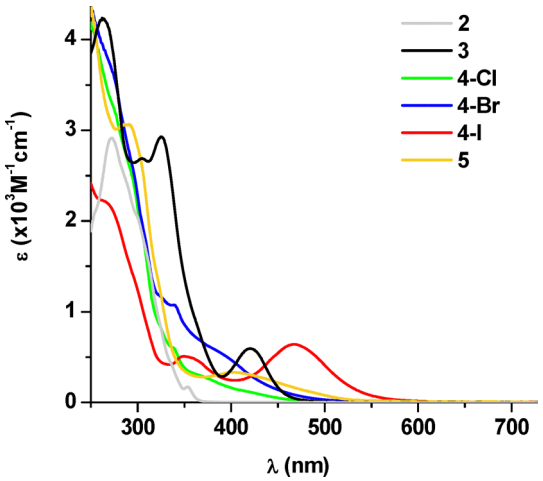

Fig. 6 UV-vis absorption spectra in CH_2Cl_2 (5×10^{-5} M).

Time-Dependent Density Functional Theory (TD-DFT) studies were performed on **3**, **4-Cl**, **4-I** and **5** (see Fig. 7 and Fig. S11, S12 and Tables S4, S5). Unrestricted geometry optimizations were performed without constraints at the level M06/MWB60(Pt)/MWB46(I)/6-31G(d)(light atoms) (see computational methods in the SI). As shown in Fig. 7, the calculated S_1 (408 nm) and S_2 (373 nm) transitions for complex **3** are in agreement with the experimentally observed UV-vis absorptions. They arise from HOMO → LUMO and HOMO → LUMO+1 transitions, respectively. The HOMO is centered at the dσ* Pt orbitals (81%) whilst the LUMO and LUMO + 1 are located on the C^C* ligand (80%). Therefore, as anticipated, the lowest energy absorptions are originated from ^{1}MMLCT [dσ*(Pt–Pt) → π*(C^C*)] states.

Like in other examples where dinuclear molecules possess strong Pt···Pt interactions,[30,31,57] the cyclic voltammogram of **3** in CH_2Cl_2 solution using Fc^+/Fc as internal redox reference (experimental details in the SI) exhibits one *quasi*-reversible

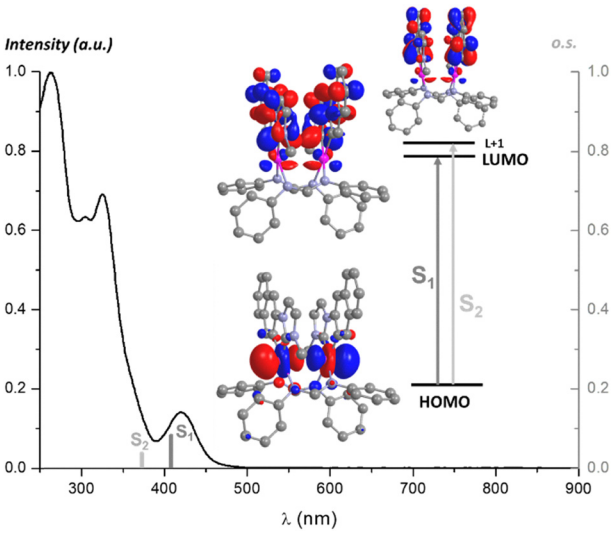

Fig. 7 Normalized absorption spectra in solution, calculated S_n transitions (gray bars), and molecular orbital plots (isoval. 0.03) for compound **3**.

oxidative peak at *ca.* −0.33 V (ΔE_p = 99 mV at 100 mV s^{-1} Table S6 and Fig. S13). The HOMO (−4.76 eV) and LUMO (−2.15 eV) energies were estimated based on the following formulae: E_{HOMO} (eV) = $-(E^{ox}_{onset} + 5.1)$ in the Fermi scale,[58] and E_{LUMO} (eV) = $E_{HOMO} + E_g$ (see Table S6).[59] The high energy level of the HOMO agrees with its dσ* character, generated by the overlap of the d_{z^2} orbitals of the two Pt(II) centers located in close proximity and with the theoretical calculations.

In the oxidized Pt complexes, in view of the minimal oscillator strength of lowest calculated singlets and the experimental absorption bands, we focused on the the S_5 and S_7 transitions for complexes **4-Cl** and **4-I**, respectively. So, by analyzing their compositions we can observe abundant orbital mixing for the halogenide derivatives (see Table S4).

Thus, to visualize these results, the natural transition orbitals (NTOs) were calculated for both. As illustrated in Fig. S11, their lowest energy absorptions would be mainly attributed to ^{1}LMMCT[π(C^C*) → dσ*(Pt–Pt)] combined with ^{1}XMMCT[π(Cl) → dσ*(Pt–Pt)] for **4-Cl** whereas for **4-I** ^{1}LMMCT with ^{1}LXCT[π(C^C*) → π*(I)] transition. For complex **5**, we study the S_2 [H-1 → LUMO (87%)] and S_3 transition [H-2 → LUMO (87%)] which are in agreement with the experimental UV-visible absorption and they would correspond mainly to mixed transitions ^{1}L′MM/RCT[π(N^N) → dσ*(Pt–Pt)/σ*(Me)] for S_2 and ^{1}LMM/RCT[π(C^C*) → dσ*(Pt–Pt)/σ*(Me)] for S_3 (see Fig. S12).

Emission properties and theoretical calculations. The photophysical properties were examined under an argon atmosphere, unless stated otherwise, and they appear listed in Table 1. The monometallic starting complex **2** displays a very weak and well-resolved vibronic emission at 472 nm in rigid matrix of 2-MeTHF (77 K) and in 2 wt% PMMA film (Fig. S14) with rather long lifetime decays, mainly attributed to ^{3}LC [C^C*] excited states. By contrast, compound **3** shows a very intense structureless band with maxima at 540 nm, in fluid solution of 2-MeTHF (10^{-3} M) (see Fig. 8). In 2 wt% PMMA film, the emission experiences a subtle rigidochromism (λ_{em}: 520 nm; 712 cm^{-1}) which is typical of charge transfer excited states.[60] This emission fits to a monoexponential decay (1.80 μs), exhibits a high quantum yield (0.90) and a full width at half maximum (FWHM) of 56 nm (2014 cm^{-1}); all these values appear to be similar to those reported for related dinuclear

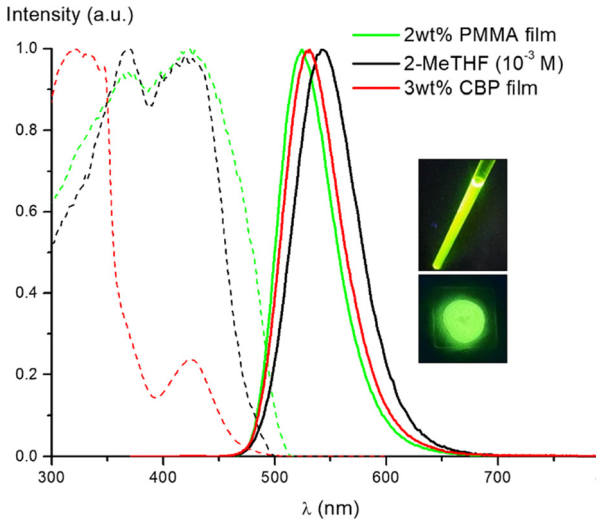

Fig. 8 Normalized excitation (---) and emission (—) spectra of **3** at 298 K. Pictures taken under 365 nm.

complexes.[35,46,48,54] The photoluminescent properties of **3** were also measured in 4,4′-bis(*N*-carbazolyl)-1,1′-biphenyl (CBP), which is the host material employed for the fabrication of OLED devices (see below). Concentrations of 1.5 wt% and 3 wt% of **3** in CBP were studied and exhibited comparable data to each other and also to those of the 2 wt% PMMA film (Fig. 8 and Table 1).

Regarding the emission characteristics and the resemblance between the excitation and absorption spectrum, we can presume that the phosphorescence arises from ^{3}MMLCT [dσ*(Pt–Pt) → π*(C^C*)] excited states. To validate this assignment, spin density distributions were calculated on the T_1 state (Fig. S15) and the Pt–Pt bonding parameters of the optimized geometries in the S_0 and T_1 states were also tabulated (Table S7). According to them, the Pt–Pt distance is shortened (0.23 Å) at the first triplet state in relation to that of the ground state, as the electron is promoted from the antibonding orbital dσ*(Pt–Pt).

As observed in related Pt_2(III,III) systems,[40,41,56,61] compounds **4-X** display phosphorescent emissions, but only in solid at 77 K, with maxima at 960, 970 and 1055 nm that are sensitive to the

Table 1 Photophysical data of Pt complexes[a]

Compound	Media (*T*/[K])	λ_{exc} (nm)	λ_{em} (nm)	τ (μs)	Φ_{PL}	$k_r \times 10^5$ (s^{-1})[f]	$k_{nr} \times 10^5$ (s^{-1})[g]
2	2-MeTHF[b] (77)	360	472_{max}, 508, 548, 596	361.0			
	2wt% PMMA	360	472_{max}, 508, 546, 588	73.0	0.05	0.007	0.1
3	2-MeTHF[c]	370, 420	540	0.61	0.45	7.4	9.0
	2wt% PMMA	370, 420	520	1.80	0.90	5.0	0.5
	1.5wt% CBP	370, 425	529	1.45	0.82	5.6	1.2
	3wt% CBP	370, 425	532	1.52	0.91	5.9	0.6
	Solid[d]	470	568	4.71	0.20	0.4	1.7
4-Cl	Solid (77)	390	960	29.7 ns	[e]		
4-Br	Solid (77)	450	970	49.1 ns	[e]		
4-I	Solid (77)	470	1055	28.2 ns	[e]		

a = Measured in Ar atmosphere and rt unless noted; *b* = 5 × 10^{-5} M; *c* = 10^{-3} M; *d* = in the air; *e* = outside the instrument's capability; *f* = $k_r = \Phi_{PL}/\tau$, *g*: $k_{nr} = (1 - \Phi_{PL})/\tau$.

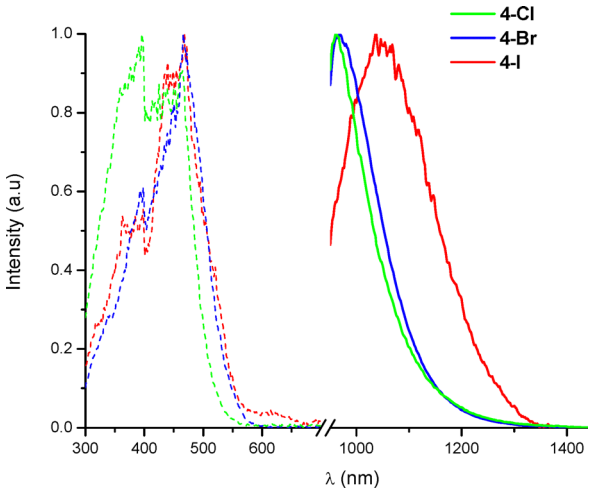

Fig. 9 Normalized excitation (---) and emission (—) spectra.

X ligand (Fig. 9). These are tentatively assigned to ^{3}XMMCT [σ(X) → dσ*(Pt–Pt)] excited states which are in close agreement with the spin density distributions and the bonding parameters of the optimized geometries in the S_0 and T_1 states (Fig. S15 and Table S7). As opposed to the **4-X** series, complex **5** shows no detectable emission in either the visible or NIR regions at 298 or 77 K. DFT calculations corroborate this observation: attempts to optimize the geometry of the T_1 were unsuccessful due to severe structural distortions occurring during the optimization process, including the dissociation of the methyl group from the metal center. Therefore, such pronounced structural deformations in T_1 could account for the lack of luminescence of complex **5**. Evaluating the emissive behaviour of these Pt_2(II,II) and Pt_2(III,III) systems relative to similar double-decker complexes with C^N-cyclometallated and N^S bridging ligands published in our group,[40,41] we noticed that the preceding derivatives appear to be weakly or non-emissive whereas the oxidized Pt(III) analogues display more intense NIR emission bands even at rt.

For compound **3**, the photophysical study was completed with time resolved photoluminescence experiments. They were recorded in 1.5 wt% and 3 wt% CBP affording similar results. Fig. S16(A and B) shows the photoluminescence spectra recorded at different delay times which were integrated to obtain the decay trace depicted in Fig. S16(C and D).

The photoluminescence lifetime was obtained using a mono-exponential fit of the decay trace. The PL recorded at early times in the first nanoseconds originates from CBP fluorescence and has been omitted in this analysis. There is a second exponential component at longer delay times which arises, as we believe from a resonance between the T_1 energy of complex **3** and CBP host. The close proximity of the T_1 states means that the T_1 of CBP (2.58 eV) can become populated from the T_1 of **3** (2.61 eV).[62,63] Following this, the T_1 of **3** can become repopulated, but with a lower rate, resulting in PL characteristic of **3**, but with a longer lifetime than what is observed when emission originates directly from **3**. A somewhat similar resonance has been previously observed between FIrpic and CBP.[64,65]

Organic light emitting diodes

In view of the excellent photophysical properties of **3** (high photoluminescence QY, short phosphorescence lifetime and relatively narrowband emission), and its high thermal stability up to 410 °C (see TGA in Fig. S17), organic light emitting devices were fabricated using this complex as the active material in the emitting layer. Various host materials and doping concentrations were tested, CBP host and emitter concentrations at 1.5 and 3% clearly yielding the best results. The complex sublimes below 250 °C, this is far below the decomposition temperature, which is above 400 °C. This is a remarkably low sublimation temperature for a complex with such a high molecular weight. The optimum device structure and thickness of the layers are given as follow and are represented in Fig. 10:

ITO | HAT-CN (10 nm) | TSBPA (40 nm) | CBP (2 nm) | CBP co 1.5 or 3% 3 (20 nm) | TmPyPB (50 nm) | LiF (0.8 nm) | Al (70 nm)

The devices use indium tin oxide (ITO) and lithium fluoride/aluminium (LiF/Al) as the anode and cathode, respectively. 1,4,5,8,9,11-Hexaazatriphenylenehexacarbonitrile (HAT-CN) is employed as a hole injection material. 4,4′-(Diphenylsilanediyl)bis(*N*,*N*-diphenylaniline) (TSBPA) and 1,3,5-tris(3-pyridyl-3-phenyl)benzene (TmPyPB) are used as the hole and electron transport layers, respectively. A thin layer of CBP is included as an additional hole transport layer. The representative device performances for a particular pixel of the 1.5 and 3% emitter OLEDs are given in Fig. 11. The device characteristics are summarised in Table 2. All values were obtained by averaging the results from at least 12 pixels. A histogram of the maximum EQE for all the pixels is given in Fig. S18. Both OLEDs show a green emission with CIE = (0.31, 0.63), λ_{EL} ~ 540 nm and FWHM of 66 nm (0.28 eV). The maximum EQE, current and power efficiency of the 1.5% device are slightly higher in comparison to the 3% device. However, the 3% device shows a clearly better efficiency roll-off at higher current densities and

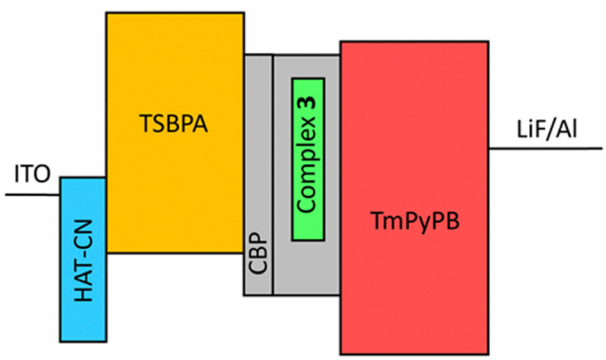

Fig. 10 Structure of the OLED devices fabricated in this work. The heights of the bars represent the HOMO and LUMO energies of the materials which comprise each layer. The width of the bars approximately represents the relative thickness of the layers.

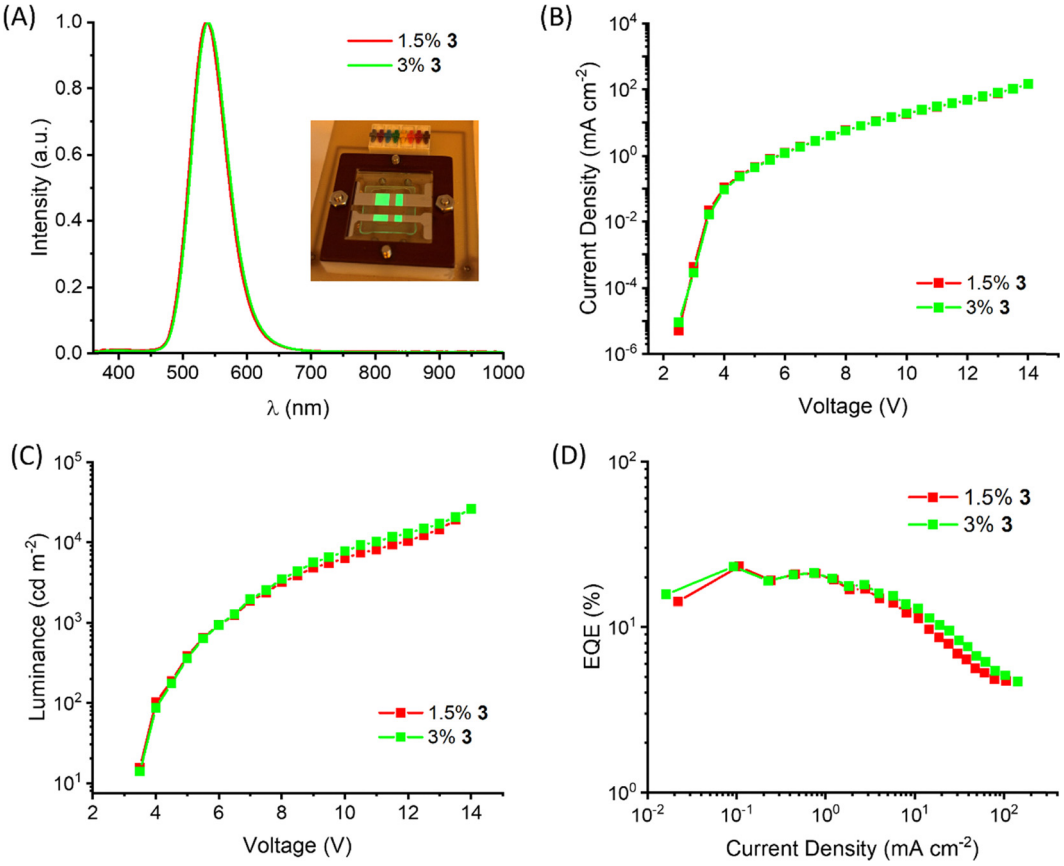

Fig. 11 Performance of the OLED devices fabricated using 1.5 or 3% of **3** in a CBP host. (A) Electroluminescence and an image of the operational device, (B) current density as a function of voltage, (C) luminescence *vs.* voltage and (D) EQE as a function of current density.

Table 2 Electrical properties of the fabricated OLED devices with **3**

Device	EQE_{avg} [a] [%]	EQE_{max} [b] [%]	V_{ON} [c] [V]	λ_{EL} [d] [nm]	L_{max} [e] [cd m^{-2}]	CE_{max} [f] [cd A^{-1}]	PE_{max} [g] [lm W^{-1}]	CIE (x, y) [h]	FWHM [i] [nm]/[eV]
1.5% **3** CBP	21.8	23.2	3	538	22 000	89.8	66.6	(0.31, 0.63)	66/0.28
3% **3** CBP	20.7	23.2	3	541	22 400	81.6	51.3	(0.33, 0.62)	66/0.28

[a] Average maximum EQE. [b] Maximum EQE from a single pixel. [c] Turn-on voltage at 1 cd m^{-2}. [d] EL maxima. [e] Maximum luminance. [f] Maximum current efficiency. [g] Maximum power efficiency. [h] Colour coordinates of the electroluminance defined by the International Commission on Illumination. [i] Full width at half maximum of the electroluminescence.

hence reach a higher luminance. In both cases, the devices show exceptional results with excellent EQE (*ca.* 22%), low turn-on voltage (3 V) and very high luminance (22 000 cd m^{-2}). These values are comparable or even superior to those reported for OLEDs based on double decker Pt complexes with μ-N^N amidinate ligands and different chromophores (C^N or C^C*): [{Pt(C^N)(μ-N^N)}$_2$] (C^N: 3,6-di-*tert*-butyl-9-(pyrimidin-2-yl)-9*H*-carbazole; λ_{em}: 598 nm; EQE: 5.3%),[31] [{Pt(C^N)(μ-N^N)}$_2$] (C^N: 5-(pyridin-2-yl)-2-(trifluoromethyl)pyrimidinate; λ_{em}: 767 nm; EQE: 0.14%)[30] and [{Pt(C^C*)(μ-N^N)}$_2$] (C^C*: pyridyl- or pyrazinyl-fused NHC; λ_{em}: 616 nm; EQE: 15.5–19.4%).[35]

As indicated, all devices exhibited red or deep red electroluminescence. Therefore, we alternatively contrasted our results with those of green OLEDs fabricated using Pt bimetallic emitters. Although these systems do not feature an identical double decker architecture, they share key structural characteristics such as C^N or C^C* cyclometallated chromophoric groups, doubly bridging ligands and pronounced metal–metal interactions. Notably, the efficiencies achieved in our devices surpass those reported for these related green OLEDs: [{Pt(C^N)(μ-Rpz)}$_2$] (Rpz = 3-methyl-5-*tert*-butylpyrazolate)[66] and [{Pt(C^C*)(μ-Rpz)}$_2$] (Rpz = 3,5-diphenylpyrazolate)[67] with EQEs of 6.0% and 10%, respectively. As noted, our system ranks among the most efficient Pt-based green emitters exhibiting excellent OLEDs performances.

Conclusions

Double decker Pt_2(II,II) complex **3** with a cyclometallated N-heterocyclic carbene and diphenylformamidinate bridging

ligands was obtained as a single isomer by treating the mononuclear bisformamidine complex **2** with NEt_3 in refluxing 2-methoxyethanol. When exposed to 365 nm light in the presence of haloforms, **3** experiences two-electron oxidation, resulting in the corresponding $Pt_2(III,III)$ complexes with halogenides as axial capping ligands. Furthermore, due to the nucleophilic character of the Pt centers in **3**, the complex readily reacted with $[Me_3O]BF_4$ affording the mixed-valence dinuclear complex $[(C\hat{}C^*)Pt^{II}(\mu\text{-}N\hat{}N)_2Pt^{IV}(C\hat{}C^*)(CH_3)]BF_4$ (**5**), with the metals involved in a donor–acceptor Pt(II) → Pt(IV) bond. Accordingly, two ^{195}Pt NMR resonances appear at −3264 and −2373 ppm with a large Pt–Pt coupling constant of 2155 Hz. X-ray analysis of **3** and **4-Cl** confirmed the *anti*-conformation and revealed short Pt–Pt separations of 2.8645 and 2.6070 Å, the latter in line with the presence of a metal–metal bond in the $Pt_2(III,III)$ core. We found several differences in the photo-emissive behaviour of these $Pt_2(II,II)$ and $Pt_2(III,III)$ systems relative to analogous double-decker complexes with C^N-cyclometallated ligands previously reported by our group. First, $Pt_2(II,II)$ complex **3** shows green emission with exceptionally higher QY. Second, the oxidized $Pt_2(III,III)$ counterparts display less intense NIR-I or NIR-II emissions in solid state at 77 K whereas the preceding C^N-derivatives were emissive in the NIR-II spectral range even at rt.

Finally, the technological applicability of this work was validated by employing compound **3** as a green emitter in vacuum-deposited OLEDs. The resulting devices exhibited outstanding performance, delivering a maximum EQE of 22%, a low turn-on voltage of 3 V, and exceptionally high luminance (22 000 cd m^{-2}), that are among the best reported for Pt-based OLEDs. Collectively, this work sets out an approachable platform from which we can introduce structural modifications to achieve tunable emitters from visible to NIR-II region.

Conflicts of interest

There are no conflicts to declare.

Data availability

The data supporting this article have been included as part of the supplementary information (SI) (.pdf, .xyz and .cif files). Supplementary information is available. See DOI: **https://doi.org/10.1039/d6qm00041j**.

CCDC 2515149–2515151 contain the supplementary crystallographic data for this paper.[68a–c]

Acknowledgements

This work was supported by Grants PID2024-155563NB-I00 funded by MICIU/AEI/10.13039/501100011033 and ERDF/EU and by the ''Gobierno de Aragon'' (Grupo E17_23R). The authors thank CESGA for generous allocation of computational resources. P. P. thanks to the National Science Centre, Poland for funding, grant No. 2022/47/D/ST4/01496.

Notes and references

1 G. Hong, X. Gan, C. Leonhardt, Z. Zhang, J. Seibert, J. M. Busch and S. Bräse, A Brief History of OLEDs—Emitter Development and Industry Milestones, *Adv. Mater.*, 2021, **33**, 2005630.
2 S. J. Zou, Y. Shen, F. M. Xie, J. D. Chen, Y. Q. Li and J. X. Tang, Recent Advances in Organic Light-Emitting Diodes: Toward Smart Lighting and Displays, *Mater. Chem. Front.*, 2020, **4**, 788–820.
3 Y. Long and H. Meng, Key Components for Active-Matrix OLED Displays: Fundamentals and Market Status, *J. Lumin.*, 2025, **280**, 121099.
4 Y.-F. Liu, J. Feng, Y.-G. Bi, D. Yin and H.-B. Sun, Recent Developments in Flexible Organic Light-Emitting Devices, *Adv. Mater. Technol.*, 2019, **4**, 1800371.
5 D. Won, J. Bang, S. H. Choi, K. R. Pyun, S. Jeong, Y. Lee and S. H. Ko, Transparent Electronics for Wearable Electronics Application, *Chem. Rev.*, 2023, **123**, 9982–10078.
6 D. Yin, S.-X. Jia, H.-Y. Zhang, S.-H. Li, Y.-F. Liu and J. Feng, Applications of Organic Light-Emitting Diodes in Wearable Electronics, *Wearable Electron.*, 2025, **2**, 215–236.
7 W. Zhang, X. Wang, J. Duan, Z. Zheng, J. Zhang, G. Hang and Z. L. Liu, Recent Research Advances in Textile-Based Flexible Power Supplies and Displays for Smart Wearable Applications, *ACS Appl. Electron. Mater.*, 2024, **6**, 5429–5455.
8 C. Murawski and M. C. Gather, Emerging Biomedical Applications of Organic Light-Emitting Diodes, *Adv. Opt. Mater.*, 2021, **9**, 2100269.
9 E. H. Cho, Y. W. Kim, J. Sim, H. Yeon, S. Baek, S. M. Jeong, J. Lee, Y. Jeon and K. C. Choi, Recent Advances in Flexible and Wearable OLEDs for Biomedical Applications: a Review, *Mater. Horiz.*, 2025, **12**, 8862–8894.
10 P. Tao, J. Jin, X. Zheng, Y.-J. Pu and W.-Y. Wong, Engineering Emissive Excited States in Organic Electroluminescent Materials, *Matter*, 2025, **8**, 102142.
11 X. L. Yang, G. J. Zhou and W. Y. Wong, Functionalization of Phosphorescent Emitters and their Host Materials by Main-Group Elements for Phosphorescent Organic Light-Emitting Devices, *Chem. Soc. Rev.*, 2015, **44**, 8484–8575.
12 M. Chaaban, C. Zhou, H. Lin, B. Chyi and B. Ma, Platinum(II) Binuclear Complexes: Molecular Structures, Photophysical Properties, and Applications, *J. Mater. Chem. C*, 2019, **7**, 5910–5924.
13 G. Li, D. Zhu, X. Wang, Z. Su and M. R. Bryce, Dinuclear Metal Complexes: Multifunctional Properties and Applications, *Chem. Soc. Rev.*, 2020, **49**, 765–838.
14 Q.-C. Zhang, H. Xiao, X. Zhang, L.-J. Xu and Z.-N. Chen, Luminescent Oligonuclear Metal Complexes and the Use in Organic Light-Emitting Diodes, *Coord. Chem. Rev.*, 2019, **378**, 121–133.
15 J.-L. Liao, P. Rajakannu, P. Gnanasekaran, S.-R. Tsai, C.-H. Lin, S.-H. Liu, C.-H. Chang, G.-H. Lee, P.-T. Chou, Z.-N. Chen and Y. Chi, Luminescent Diiridium Complexes with Bridging Pyrazolates: Characterization and Fabrication of OLEDs Using Vacuum Thermal Deposition, *Adv. Opt. Mater.*, 2018, **6**, 1800083.

16 M. Z. Shafikov, R. Daniels and V. N. Kozhevnikov, Unusually Fast Phosphorescence from Ir(III) Complexes via Dinuclear Molecular Design, *J. Phys. Chem. Lett.*, 2019, **10**, 7015–7024.
17 H. Yersin, A. F. Rausch, R. Czerwieniec, T. Hofbeck and T. Fischer, The triplet State of Organo-Transition Metal Compounds. Triplet harvesting and Singlet Harvesting for Efficient OLEDs, *Coord. Chem. Rev.*, 2011, **255**, 2622–2652.
18 Y. Xiao, H. Wang, Z. Xie, M. Shen, R. Huang, Y. Miao, G. Liu, T. Yu and W. Huang, NIR TADF Emitters and OLEDs: Challenges, Progress, and Perspectives, *Chem. Sci.*, 2022, **13**, 8906–8923.
19 M.-P. Zhuo, X.-D. Wang and L.-S. Liao, Recent Progress of Novel Organic Near-Infrared-Emitting Materials, *Small Sci.*, 2022, **2**, 2200029.
20 P. L. dos Santos, P. Stachelek, Y. Takeda and P. Pander, Recent Advances in Highly-Efficient Near Infrared OLED Emitters, *Mater. Chem. Front.*, 2024, **8**, 1731–1766.
21 V. Sicilia, J. Forniés, J. M. Casas, A. Martin, J. A. López, C. Larraz, P. Borja, C. Ovejero, D. Tordera and H. Bolink, Highly Luminescent Half-Lantern Cyclometalated Platinum(II) Complex: Synthesis, Structure, Luminescence Studies, and Reactivity, *Inorg. Chem.*, 2012, **51**, 3427–3435.
22 M. Yoshida and M. Kato, Regulation of Metal–Metal Interactions and Chromic Phenomena of Multi-Decker Platinum Complexes Having π-Systems, *Coord. Chem. Rev.*, 2018, **355**, 101–115.
23 X. Wu, Y. Liu, Y. Wang, L. Wang, H. Tan, M. Zhu, W. Zhu and Y. Cao, Highly Efficient Near-Infrared Emission from Binuclear Cyclometalated Platinum Complexes Bridged with 5-(4-octyloxyphenyl)-1,3,4-oxadiazole-2-thiol in PLEDs, *Org. Electron.*, 2012, **13**, 932–937.
24 W. Xiong, F. Meng, H. Tan, Y. Wang, P. Wang, Y. Zhang, Q. Tao, S. Su and W. Zhu, Dinuclear Platinum Complexes Containing Aryl-isoquinoline and Oxadiazole-thiol with an Efficiency of over 8.8%: in-depth Investigation of the Relationship between their Molecular Structure and Near-Infrared Electroluminescent Properties in PLEDs, *J. Mater. Chem. C*, 2016, **4**, 6007.
25 N. Su, F. Meng, P. Wang, X. Liu, M. Zhu, W. Zhu, S. Su and J. Yu, Near-Infrared Emission from Binuclear Platinum (II) Complexes Containing Pyrenylpyridine and Pyridylthiolate Units: Synthesis, Photo-physical and Electroluminescent Properties, *Dyes Pigm.*, 2017, **138**, 162–168.
26 W. Xiong, F. Meng, C. You, P. Wang, J. Yu, X. Wu, Y. Pei, W. Zhu, Y. Wang and S. Su, Molecular Isomeric Engineering of Naphthyl-Quinoline-Containing Dinuclear Platinum Complexes to Tune Emission from Deep Red to Near Infrared, *J. Mater. Chem. C*, 2019, **7**, 630–638.
27 P. Rajakannu, W. Lee, S. Park, H. S. Kim, H. Mubarok, M. H. Lee and S. Yoo, Molecular Engineering for Shortening the Pt···Pt Distances in Pt(II) Dinuclear Complexes and Enhancing the Efficiencies of these Complexes for Application in Deep-Red and Near-IR OLEDs, *Adv. Funct. Mater.*, 2023, **33**, 2211853.
28 J. Yu, X. Yang, J. Chen, D. Liu, L. Cao, H. Tan and W. Zhu, Achieving Near-Infrared Electroluminescence Around 780 nm Based on Butterfly-Shaped Dinuclear Platinum(II) Complexes, *J. Mater. Chem. C*, 2023, **11**, 12384–12391.
29 I. Gil-Gómez de Segura, D. Gómez de Segura, M. Hasler, M. T. Moreno, E. Lalinde, M. Nieddu, R. D. Costa and J. Fernandez-Cestau, Half-lantern Pt(II) Complexes in Deep-red Hybrid Light-Emitting Diodes, *J. Mater. Chem. C*, 2025, **13**, 15002–15012.
30 S. F. Wang, L.-W. Fu, Y.-C. Wei, S. Liu, J. Lin, G. Lee, P.-T. Chou, J. Huang, C.-I. Wu, Y. Yuan, C.-S. Lee and Y. Chi, Near-Infrared Emission Induced by Shortened Pt–Pt Contact: Diplatinum(II) Complexes with Pyridyl Pyrimidinato Cyclometalates, *Inorg. Chem.*, 2019, **58**, 13892–13901.
31 H. Yao, L. Qiao, L. Yuan, X. Luan, Y. Shen, Y. Zhang, L. Zhou and H. Bian, Synthesis of Phosphorescent Syn, Anti-Isomeric Clamshell Platinum(II) Dimers for OLED Applications, *J. Mater. Chem. C*, 2024, **12**, 4473–4483.
32 Y. M. Zhang, J. S. Miao, J. F. Xiong, K. Li and C. L. Yang, Rigid Bridge-Confined Double-Decker Platinum(II) Complexes Towards High-Performance Red and Near-Infrared Electroluminescence, *Angew. Chem., Int. Ed.*, 2022, **61**, e202113718.
33 L. Wang, Z. Wen, Y. Xu, Y. Zhang, J. Miao, Z. Chen and K. Li, High-Efficiency and Stable Red to Near-Infrared Organic Light-Emitting Diodes Using Dinuclear Platinum(II) Complexes, *Mater. Chem. Front.*, 2023, **7**, 873–880.
34 Z. Wen, Y. Xu, X. Song, J. S. Miao, Y. Zhang, K. Li and C. L. Yang, Approaching the Shortest Intermetallic Distance of Half-Lantern Diplatinum(II) Complexes for Efficient and Stable Deep-Red Organic Light-Emitting Diodes, *Adv. Optic. Mater.*, 2023, **11**, 2300201.
35 M. Xue, T. L. Lam, G. Cheng, W. Liu, K. H. Low, L. Du, S. Xu, F. F. Hung, D. L. Phillips and C. M. Che, Exceedingly Stable Luminescent Dinuclear Pt(II) Complexes with Ditopic Formamidinate Bridging Ligands for High-Performance Red and Deep-Red OLEDs with LT97 up to 2446 h at 1000 cd m^{-2}, *Adv. Opt. Mater.*, 2022, **10**, 2200741.
36 K.-W. Lo, C.-H. Tsang, S. Xu, G. Cheng, X. Chang, L. Duan and C.-M. Che, Stable Binuclear Platinum(II) Emitters with Substituted 2-Hydroxypyridine Bridging Ligands for Red and Near-Infrared OLEDs with EQE up to 32% and LT95 up to 26250h at 1000cd m^{-2}, *Angew. Chem., Int. Ed.*, 2025, e19762.
37 V. Sicilia, P. Borja, J. M. Casas, S. Fuertes and A. Martin, Selective Synthesis of New Half-Lantern Benzoquinolate Platinum Complexes. DFT and Photophysical Studies on the Platinum (II,II) Derivative, *J. Organomet. Chem.*, 2013, **731**, 10–17.
38 V. Sicilia, M. Baya, P. Borja and A. Martín, Oxidation of Half-Lantern Pt_2(II,II) Compounds by Halocarbons. Evidence of Dioxygen Insertion into a Pt(III)-CH_3 Bond, *Inorg. Chem.*, 2015, **54**, 7316–7324.
39 V. Sicilia, P. Borja and A. Martín, Half-Lantern Pt(II) and Pt(III) Complexes. New Cyclometalated Platinum Derivatives, *Inorganics*, 2014, **2**, 508–523.
40 I. Melendo, S. Fuertes, A. Martín and V. Sicilia, NIR-II Emission from Cyclometalated Dinuclear Pt(III) Complexes, *Inorg. Chem.*, 2024, **63**, 5470–5480.

41 I. Melendo, P. Borja, S. Fuertes, A. Martín and V. Sicilia, Double-Decker Platinum Complexes: From Visible to NIR-II Luminescence, *Inorg. Chem.*, 2025, **64**, 17523–17532.
42 C. Cebrian and M. Mauro, Recent Advances in Phosphorescent Platinum Complexes for Organic Light-Emitting Diodes, *Beilstein J. Org. Chem.*, 2018, **14**, 1459–1481.
43 I. Melendo, J. Camacho-Aguayo, S. Paziresh, S. Fuertes, A. Martín, S. de Marcos, J. Galbán and V. Sicilia, A Cyclometalated N-Heterocyclic Carbene and Acetylacetonate Ligands in a Phosphorescent Pt(II) Dye for Sensing Glucose, *Dyes Pigm.*, 2023, **219**, 111630.
44 L. Arnal, S. Fuertes, A. Martín, M. Baya and V. Sicilia, A Cyclometalated N-Heterocyclic Carbene: The Wings of the First Pt_2(II,II) Butterfly Oxidized by CHI_3, *Chem. – Eur. J.*, 2018, **24**, 18743–18748.
45 V. Sicilia, L. Arnal, D. Escudero, S. Fuertes and A. Martin, Chameleonic Photo- and Mechanoluminescence in Pyrazolate-Bridged NHC Cyclometalated Platinum Complexes, *Inorg. Chem.*, 2021, **60**, 12274–12284.
46 H. Leopold, M. Tenne, A. Tronnier, S. Metz, I. Muenster, G. Wagenblast and T. Strassner, Binuclear CC Cyclometalated Platinum(II) NHC Complexes with Bridging Amidinate Ligands, *Angew. Chem., Int. Ed.*, 2016, **55**, 15779–15782.
47 S. Stipurin and T. Strassner, Phosphorescent Bimetallic C ∧ C Platinum(II) Complexes with Bridging Substituted Diphenylformamidinates, *Chem. – Eur. J.*, 2022, **28**, e202202227.
48 L. Yuan, H. Yao, Y. Shen and Y. Zhang, A Cyclometalated Pt(II)–Pt(II) Clamshell Dimer with a Triplet Emission at 887 nm, *Dalton Trans.*, 2024, **53**, 5125–5132.
49 P. Fan, L. Yuan and Y. Zhang, Heteronuclear Pt^{II}-Pd^{II} Dimers Formation Through Ligands Subtle Tailoring, *Inorg. Chem. Front.*, 2025, **12**, 1812–1821.
50 K. Umakoshi, I. Kinoshita, A. Ichimura and S. Ooi, Binuclear Platinum(II) and -(III) Complexes of Pyridine-2-Thiol and its 4-Methyl Analog. Synthesis, Structure, and Electrochemistry, *Inorg. Chem.*, 1987, **26**, 3551–3556.
51 H. R. Shahsavari, E. Lalinde, M. T. Moreno, M. Niazi, S. H. Kazemi, S. Abedanzadeh, M. Barazandeh and M. R. Halvagar, Half-Lantern Cyclometalated Pt(II) and Pt(III) Complexes with Bridging Heterocyclic Thiolate Ligands: Synthesis, Structural Characterization, and Electrochemical and Photophysical Properties, *New J. Chem.*, 2019, **43**, 7716–7724.
52 L. Arnal, D. Escudero, S. Fuertes, A. Martin and V. Sicilia, High-Valent Pyrazolate-Bridged Platinum Complexes: A Joint Experimental and Theoretical Study, *Inorg. Chem.*, 2022, **61**, 12559–12569.
53 V. Sicilia, L. Arnal, S. Fuertes, A. Martin and M. Baya, Metal-Metal Cooperation in the Oxidation of a Flapping Platinum Butterfly by Haloforms: Experimental and Theoretical Evidence, *Inorg. Chem.*, 2020, **59**, 12586–12594.
54 F. Wurl, S. Stipurin, J. I. Kollar and T. Strassner, Synthesis and Photophysical Properties of Monometallic C^C* Platinum(II) Formamidinate Complexes using Sterically Demanding Ligands, *Angew. Chem., Int. Ed.*, 2023, **62**, e202301225.
55 Z. Wang, L. Jiang, Z.-P. Liu, C. R. R. Gan, Z. L. Liu, X. H. Zhang, J. Zhao and T. S. A. Hor, Facile Formation and Redox of Benzoxazole-2-Thiolate-Bridged Dinuclear Pt(II/III) Complexes, *Dalton Trans.*, 2012, **41**, 12568–12576.
56 X. Wu, D.-G. Chen, D. Liu, S.-H. Liu, S.-W. Shen, C.-I. Wu, G. Xie, J. Zhou, Z.-X. Huang, C.-Y. Huang, S.-J. Su, W. Zhu and P.-T. Chou, Highly Emissive Dinuclear Platinum(III) Complexes, *J. Am. Chem. Soc.*, 2020, **142**, 7469–7479.
57 A. Chakraborty, J. C. Deaton, A. Haefele and F. N. Castellano, Charge-Transfer and Ligand -Localized Photophysics in Luminescent Cyclometalated Pyrazolate-Bridged Dinuclear Platinum(II), *Organometallics*, 2013, **32**, 3819–3829.
58 C. M. Cardona, W. Li, A. E. Kaifer, D. Stockdale and G. C. Bazan, Electrochemical Considerations for Determining Absolute Frontier Orbital Energy Levels of Conjugated Polymers for Solar Cell Applications, *Adv. Mater.*, 2011, **23**, 2367–2371.
59 Y. Yan, Z. Yu, C. Liu and X. Jin, Effects of Phenyl/Thienyl Substituents at Acetylacetone Auxiliary Ligands on the Properties of Cyclometalated Platinum(II) Complexes, *Dyes Pigm.*, 2020, **173**, 107949.
60 J. S. McCarthy, M. J. McCormick, J. H. Zimmerman, H. R. Hambrick, W. M. Thomas, C. D. McMillen and P. S. Wagenknecht, Role of the Trifluoropropynyl Ligand in Blue-Shifting Charge-Transfer States in Emissive Pt Diimine Complexes and an Investigation into the PMMA-Imposed Rigidoluminescence and Rigidochromism, *Inorg. Chem.*, 2022, **61**, 11366–11376.
61 M. A. Bennett, S. K. Bhargava, E. C.-C. Cheng, W. H. Lam, T. K.-M. Lee, S. H. Priver, J. Wagler, A. C. Willis and V. W.-W. Yam, Unprecedented Near-Infrared (NIR) Emission in Diplatinum(III) (d(7)-d(7)) Complexes at Room Temperature, *J. Am. Chem. Soc.*, 2010, **132**, 7094–7103.
62 V. Jankus, C. Winscom and A. P. Monkman, The Photophysics of Singlet, Triplet, and Degradation Trap States in 4,4-N,N′-Dicarbazolyl-1,1′-biphenyl, *J. Chem. Phys.*, 2009, **130**, 074501.
63 P. Schrögel, N. Langer, C. Schildknecht, G. Wagenblast, C. Lennartz and P. Strohriegl, Meta-linked CBP-Derivatives as Host Materials for a Blue Iridium Carbene Complex, *Org. Electron.*, 2011, **12**, 2047–2055.
64 H. Yersin, Highly Efficient OLEDs with Phosphorescent Materials, 2008.
65 I. Tanaka, Y. Tabata and S. Tokito, Energy-Transfer and Light-Emission Mechanism of Blue Phosphorescent Molecules in Guest-Host Systems, *Chem. Phys. Lett.*, 2004, **400**, 86–89.
66 B. Ma, P. I. Djurovich, S. Garon, B. Alleyne and M. E. Thompson, Platinum Binuclear Complexes as Phosphorescent Dopants for Monochromatic and White Organic Light-Emitting Diodes, *Adv. Funct. Mater.*, 2006, **16**, 2438–2446.
67 J. Roy, M. Forzatti, L. Arnal, A. Martin, S. Fuertes, D. Tordera and V. Sicilia, Pyrazolate-Bridged NHC Cyclometalated Pt_2 Complexes and $Pt_2Ag(PPh_3)^+$ Clusters in Electroluminescent Devices, *Inorg. Chem.*, 2024, **63**, 7275–7285.
68 (*a*) CCDC 2515149: Experimental Crystal Structure Determination, 2026, DOI: **10.5517/ccdc.csd.cc2qf6v7**; (*b*) CCDC 2515150: Experimental Crystal Structure Determination, 2026, DOI: **10.5517/ccdc.csd.cc2qf6w8**; (*c*) CCDC 2515151: Experimental Crystal Structure Determination, 2026, DOI: **10.5517/ccdc.csd.cc2qf6x9**.